Journal of Power Sources 215 (2012) 77–88

Contents lists available at SciVerse ScienceDirect

Journal of Power Sources

journal homepage: www.elsevier.com/locate/jpowsour

Kinetics of oxygen reduction reaction on nanostructured thin-film platinum alloy catalyst

R.K. Ahluwalia [a,*], X. Wang [a], A. Lajunen [b], A.J. Steinbach [c], S.M. Hendricks [c], M.J. Kurkowski [c], M.K. Debe [c]

[a] Argonne National Laboratory, Argonne, IL 60439, USA
[b] Aalto University, School of Engineering, Aalto, Finland
[c] 3M Fuel Cell Components Program, St. Paul, MN, USA

HIGHLIGHTS

- ► Nanostructured thin-film ternary PtCoMn cathode catalyst.
- ► Pressure and relative humidity dependence of oxygen–reduction reaction kinetics.
- ► 39.5 kJ mol^{-1} activation energy for ORR kinetics.
- ► 0.13–0.25 A mg_{Pt}^{-1} mass activity at 0.9 V, 1 atm H_2 and O_2, 80 °C and 100% RH.
- ► 1.7–2.0 mA cm_{Pt}^{-2} specific activity at 0.9 V, 1 atm H_2 and O_2, 80 °C and 100% RH.

ARTICLE INFO

Article history:
Received 6 February 2012
Received in revised form
24 April 2012
Accepted 26 April 2012
Available online 4 May 2012

Keywords:
Polymer electrolyte fuel cells
Alloy catalysts
Oxygen reduction reaction kinetics
Mass activity
Specific activity

ABSTRACT

The kinetics of the oxygen reduction reaction (ORR) on nanostructured thin-film (NSTF) ternary PtCoMn catalyst was investigated in 50 cm^2 proton-exchange membrane single cell fixtures. The investigation covered a wide range of oxygen partial pressures (0.2–0.5 atm), temperatures (30–90 °C), relative humidities (25–100%), and Pt loadings (0.05–0.2 mg cm^{-2}) in the cathode catalyst. The kinetic data were derived from cell polarization curves measured during Galvanodynamic scans from near open-circuit to a high current density and back to near open-circuit. The kinetic data were correlated with a single Tafel equation and a transfer coefficient that is a function of the relative humidity (RH). The correlation indicates a 0.36 order for the O_2 partial pressure, 39.5 kJ mol^{-1} activation energy for the temperature dependence, and an additional 0.9 order for RH dependence. The calculated mass activities and specific activities at 0.9 V Ohmic resistance corrected cell voltage, 1 atm H_2 and O_2 partial pressures, 80 °C and 100% RH agree well with the measured values of 0.13–0.25 A mg_{Pt}^{-1} and 1.7–2.0 mA cm_{Pt}^{-2} for the cells with different Pt loading.

Published by Elsevier B.V.

1. Introduction

Nanostructured thin film electrocatalysts have shown promise in addressing the performance, cost and durability barriers that must be overcome for mass commercialization of automotive fuel cells. Several studies by Debe and associates [1–3] have demonstrated that the NSTF catalysts can have significantly higher specific activity and durability than the conventional carbon supported highly dispersed Pt catalysts. The NSTF catalysts are formed by vacuum sputter-deposition of catalyst alloys onto a supported monolayer of highly oriented crystalline organic-pigment whiskers [1]. The support whiskers have a high aspect ratio (20–50), 0.6–2 μm length, rectangular lath-like morphology, 55 ± 12 nm width and 27 ± 7 nm thickness, and 3–5 × 10^9 cm^{-2} a real number density [1]. The whiskers have been coated with pure Pt as well as binary and ternary Pt alloys [2,3]. The PtCoMn ternary alloy (nominal 68:29–30:2–3 atomic ratio) is of particular interest as it has been evaluated extensively for performance and durability under potential cycling conditions (cyclic voltammetry with H_2/N_2), long holds at 1.5 V and higher potentials (support stability), and startups and shutdowns in H_2/air [4,5].

The purpose of this work is to characterize the activity of the ternary $Pt_{0.68}Co_{0.3}Mn_{0.02}$ NSTF catalyst for the oxygen reduction reaction (ORR) in H_2/air fuel cells. The intent is to determine the ORR activity as a function of the oxygen partial pressure, temperature, relative humidity and Pt loading. Previous studies on the ORR activities of Pt and PtCoMn catalysts on NSTF whiskers have used the rotating ring-disk electrode (RRDE) method in 0.1 M $HClO_4$ at

* Corresponding author. Tel.: +1 630 252 5979; fax: +1 630 252 3296.
E-mail address: walia@anl.gov (R.K. Ahluwalia).

0378-7753/$ – see front matter Published by Elsevier B.V.
doi:10.1016/j.jpowsour.2012.04.077

room temperature to 60 °C [6]. These studies have shown that the area specific activity of Pt/NSTF is similar to that of bulk Pt and that the activity of the ternary PtCoMn catalyst is about twice the activity of Pt/NSTF. The observed enhancement in the ORR activity in the RRDE measurements is similar to the results obtained in 50 cm^2 H_2/air fuel cells [6–10].

Our approach to determine the ORR kinetics for PtCoMn/NSTF from the polarization curves for H_2/air fuel cells benefits greatly from similar work described in literature on dispersed Pt/C electrodes. The past work has relied on holding the cell at a constant potential for 10 min or longer to ensure that the catalyst reaches the corresponding equilibrium Pt oxide coverage [11]. The advantage of using long hold times is that the data are quite reproducible; the disadvantage is that the data cannot be directly used to analyze the polarization curves that are generally obtained at faster scan rates. We used a slightly different approach of holding for 2 min at each data point and averaging the potentials measured during downscans from 0.02 to 2 A cm^{-2} and reverse upscans from 2 to 0.02 A cm^{-2} (10 points per decade) to estimate cell voltages at conditions approaching the equilibrium oxide coverages. Future work will explicitly determine the oxide coverage in the ternary catalyst as a function of the cathode potentials, the effect of the oxide coverage on the ORR activity, and the dynamics of Pt oxidation and Pt oxide reduction.

2. Experimental

Eight 50 cm^2 active area single cells were assembled with a 24 μm membrane (850 equivalent weight), the ternary NSTF catalyst, and 3 M gas diffusion layers (GDL) into a Fuel Cell Technologies test cell containing quad serpentine flow fields. The GDL consisted of a backing paper to which was applied a hydrophobic treatment and an MPL (micro-porous layer). All cells had a Pt loading of 0.05 mg cm^{-2} in the anode. Two of the eight cells had a Pt loading of 0.103 mg cm^{-2} in the cathode. The Pt loading in the cathode in the other cells (two each) was 0.054, 0.146 and 0.186 mg cm^{-2}. All cells were first conditioned using a "thermal cycling" process, described in detail in Steinbach et al. [12], which consisted of repeated temperature and voltage cycles over a period of 2–3 days until stable performance was reached. Next, oxygen reduction activity of the cathode catalyst, short resistance and H_2 crossover, and electrochemically active surface area (ECSA) of cathode catalyst were measured, after which a series of tests were conducted, as described below.

Table 1 lists the baseline Pt loading in the electrodes and the operating conditions. One of the cells with 0.103 mg cm^{-2} Pt loading in the cathode was considered as the reference. The reference operating conditions were 80 °C cell temperature, 1.5 atm H_2 and air inlet pressures, 65 °C inlet dew point temperatures, and H_2 and O_2 stoichiometries (SR) of 2.

Table 2 summarizes the test matrix with eight series of tests. Series 1 tests varied the cell temperature from 75 °C to 90 °C (P = 1.5 atm, SR_c = 2, SR_a = 2) with the inlet dew points predetermined as a function of pressure, temperature and anode/cathode stoichiometry to maintain 100% relative humidity (RH) at cell exit. In all tests, humidification water was injected directly into the anode and cathode feed streams to reach the set dew points. Also, the outlet RH was not measured but was estimated from the cell operating conditions.

The backpressure regulator was used to vary the cell inlet pressure in Series 2 tests from 1 to 2.5 atm (T = 80 °C, SR_c = 2, SR_a = 2). As explained later, the target inlet pressure could not be reached under some conditions even with the backpressure valve completely open to the ambient. As in Series 1 tests, the inlet dew points were also adjusted to maintain 100% RH at cell exit.

Series 3 tests varied the inlet dew points from dry (no water addition) to 80 °C (P = 1.5 atm, T = 80 °C, SR_c = 2, SR_a = 2). Series 5 tests varied the O_2 stoichiometery from 1.5 to 5 with the inlet dew points adjusted to maintain 100% RH at cell exit (P = 1.5 atm, T = 80 °C, SR_a = 2). Series 6 tests varied the H_2 stoichiometry from 1.2 to 5 with the dew points held at the reference value of 65 °C (P = 1.5 atm, T = 80 °C, SR_c = 2). Series 7 tests were designed to investigate the cell operation during warm-up at 30, 45 and 60 °C with dry feeds (P = 1.5 atm, SR_c = 2, SR_a = 2). Similarly, Series 8 tests were designed to investigate cell operation during idling at low pressures and high O_2 stoichiometries.

Series 4 tests were conducted on cells with different Pt loadings in the cathode. These cells were only operated at the reference conditions.

To check for cell-to-cell variability, all tests were repeated on the companion cells with identical Pt loadings in the cathode.

Fig. 1a–h present the polarization curves for the eight series of tests. These were obtained during Galvanodynamic scans (GDS) at cell current densities varying from 0.02 to 2 A cm^{-2}. Only the data up to 1 A cm^{-2} are plotted in Fig. 1 since significant mass transfer effects are present at higher current densities. Our procedure was to start the measurements near the open circuit at 0.02 A cm^{-2}, then increase the current density in steps until either 2 A cm^{-2} was reached or the cell voltage decreased to 0.40 V, followed by an upscan back to 0.02 A cm^{-2}. The cell voltages were measured at ten current steps per decade but the maximum step size was limited to 0.1 A cm^{-2}. The cell was held for 120 s at each current step and the cell voltage was recorded every 5 s. Also, the cell resistance was determined every 5 s by on-line AC impedance measurements between 10 and 1 kHz, from which the high frequency resistance (HFR) was estimated by fitting to a Randle's cell model. The cell voltages presented in Fig. 1 are the measured values averaged over the last 30 s at the set current densities.

Prior to the start of the experiments, the electrochemical surface areas were determined by cyclic voltammetry (CV) between 0.085 and 0.65 V (vs. RHE) at 100 mV s^{-1} scan rate, with H_2/N_2 at 70 °C, 70 °C dew points and ambient pressure. ECSA values were determined by averaging the oxidative and reductive H_{UPD} peak areas from 100 CVs and assuming a 210 μC cm_{Pt}^{-2} charge-to-area conversion factor. The measured ECSA values, listed in Table 3, decrease from 12.4 m^2 g^{-1} at 0.054 mg cm^{-2} Pt loading to ~7 m^2 g^{-1} at 0.186 mg cm^{-2} Pt loading, and are five to ten times smaller than the ECSA of highly dispersed Pt/C (55–70 m^2 g^{-1} for Pt/C with 0.4 mg cm^{-2} Pt loading).

Table 3 includes the surface enhancement factors (SEF) obtained by multiplying the measured ECSA by the Pt loading. The SEF ($cm_{Pt}^2.cm^{-2}$) grows with increase in Pt loadings at a rate that is less than linear. Also included in Table 3 are the thicknesses of the catalyst layers as measured from SEM cross-sectional images of the NSTF catalyst-coated membranes [10]. These NSTF catalyst layers are only about one-tenth as thick as the conventional Pt/C catalysts with similar Pt loadings.

Hydrogen crossover current density and cell short resistance were determined by measuring the plateau currents between 0.4 and 0.6 V cell potentials with saturated H_2/N_2 at 1.5 atm total pressure and 80 °C cell temperature. Table 2 shows that the H_2

Table 1
Reference Pt loading in electrodes and cell operating conditions. The outlet RH is 100% at all reference operating conditions.

L_{Pt} (c) mg.cm^{-2}	L_{Pt} (a) mg.cm^{-2}	T°C	T_{DP}(c)°C	T_{DP} (a)°C	P atm	SR(c)	SR(a)
0.1	0.05	80	65	65	1.5	2	2

Table 2
Pt loading and cell operating conditions for test series 1–8.

Test Series 1: Effect of temperature								
Pt loading: 0.1(c), 0.05(a) mg.cm^{-2}; Pressure:1.5 atm; SR: 2(c), 2(a)								
	Run 1.1	Run 1.2	Run 1.3	Run 1.4	Run 1.5			
Temperature,°C	75	80	85	90	95			
Dew point T(c),°C	55	65	74	82	89			
Dew point T(a),°C	55	65	74	82	89			
Test Series 2: Effect of pressure								
Pt loading: 0.1(c), 0.05(a) mg.cm^{-2}; Temperature: 80 °C; 1.5 atm; SR: 2(c), 2(a)								
	Run 2.1	Run 2.2	Run 2.3	Run 2.4	Run 2.5			
Dew point T(c),°C	73	70	65	56	40			
Dew point T(a),°C	73	70	65	56	40			
Pressure, atm	1	1.25	1.5	2	2.5			
Test Series 3: Effect of relative humidity								
Pt loading: 0.1(c), 0.05(a) mg.cm^{-2}; Temperature: 80 °C; Pressure:1.5 atm; SR: 2(c), 2(a)								
	Run 3.1	Run 3.2	Run 3.3	Run 3.4	Run 3.5	Run 3.6	Run 3.7	Run 3.8
Dew point T(c),°C	0	50	55	60	65	70	75	80
Dew point T(a),°C	0	50	55	60	65	70	75	80
Test Series 4: Effect of platinum loading								
Temperature: 80 °C; Dew point: 65 °C(c), 65 °C(a); Pressure:1.5 atm; SR: 2(c), 2(a)								
	Run 4.1	Run 4.2	Run 4.3	Run 4.4				
Pt loading(c), mg.cm^{-2}	0.05	0.1	0.15	0.2				
Pt loading(a), mg.cm^{-2}	0.05	0.05	0.05	0.05				
Test Series 5: Effect of cathode stoichiometry								
Pt loading: 0.1(c), 0.05(a) mg.cm^{-2}; Temperature: 80 °C; Pressure:1.5 atm;								
	Run 5.1	Run 5.2	Run 5.3	Run 5.4				
Dew point T(c),°C	60	65	68	75				
Dew point T(a),°C	60	65	68	75				
SR(c)	1.5	2	2.5	5				
SR(a)	2	2	2	2				
Test Series 6: Effect of anode stoichiometry								
Pt loading: 0.1(c), 0.05(a) mg.cm^{-2}; Temperature: 80 °C; Dew point: 65 °C(c), 65 °C(a); Pressure:1.5 atm;								
	Run 6.1	Run 6.2	Run 6.3	Run 6.4	Run 6.5			
SR(c)	2	2	2	2	2			
SR(a)	1.2	1.5	2	2.5	5			
Test Series 7: Cold temperatures								
Pt loading: 0.1(c), 0.05(a) mg.cm^{-2}; Pressure:1.5 atm; SR: 2(c), 2(a)								
	Run 7.1	Run 7.2	Run 7.3					
Temperature,°C	30	45	60					
Dew point T(c),°C	0	0	0					
Dew point T(a),°C	0	0	0					
Test Series 8: Idle operation								
Pt loading: 0.1(c), 0.05(a) mg.cm^{-2}; Temperature: 80 °C; Dew point: 80 °C(c), 80 °C(a);								
	Run 8.1	Run 8.2	Run 8.3	Run 8.4				
Pressure, atm	1.05	1.1	1.2	1.3				
SR(c)	10	5	2.5	1.75				
SR(a)	2	2	2	2				

crossover current density of the membrane at these pressure and temperature conditions was about 2.4–3.5 mA cm^{-2} and the short resistance of the eight cells varied between 182 and 933 Ω cm^2.

Table 3 lists the mass activities of Pt in each cell measured in H_2/O_2 at 80 °C, 1 atm reactant H_2 and O_2 pressures and 100% RH. The mass activity measurement was made by first reducing the cathode with a 15 min hold under H_2/N_2 at ~0.10 V, after which the cathode was switched to O_2 and the cathode potential was then immediately held at 0.90 V for 20 min. The listed mass activity values are the current densities, adjusted for H_2 crossover and shorting currents, at a cell voltage of 0.9 V after 17.5 min. The measured mass activity is 0.18 A.mg$_{Pt}^{-1}$ for the reference cell with 0.103 mg cm^{-2} Pt loading and is somewhat higher in cells with lower Pt loading. This value may be compared with the 0.13 A mg$_{Pt}^{-1}$ mass activity of 47% Pt/C (TKK) reported by Neyerlin et al. [11] and 0.1 A mg$_{Pt}^{-1}$ mass activity of TKK PtCo dispersed on corrosion resistant (CR) carbon as reported by Wagner et al. [13]. Thus, as noted in earlier publications, the mass activity of ternary PtCoMn/NSTF is 40% higher than Pt/C in spite of the much lower ECSA and 80% higher than PtCo/CR-carbon [6,7]. The reason for this result is the much higher specific activity of PtCoMn/NSTF. Table 3 shows that the ternary NSTF catalyst has a specific activity between 1.7 and 2 mA.cm$_{Pt}^{-2}$, which is 6–8 times the reported values of 0.25 mA cm$_{Pt}^{-2}$ for Pt/C and 0.3 mA cm$_{Pt}^{-2}$ for PtCo/CR-carbon [13].

3. Kinetics of oxygen reduction reaction

We investigated the ORR kinetics by analyzing the polarization data for low current densities, $i < 0.5$ A cm^{-2}, where the mass transfer effects are negligible. We averaged the cell potentials measured during the upscans and downscans in order to remove any non-equilibrium effects caused by the finite Pt oxidation kinetics. We assessed the effect of the finite kinetics of Pt oxidation and PtO reduction near the open-circuit potentials by running polarization tests at the reference conditions with 10 min hold at each data point. The data showed only small and random differences between the cell voltages measured with 2 min and 10 min hold times. We excluded $i < 0.1$ A cm^{-2} polarization data while determining the ORR rate constants for three reasons. First, our analysis procedure involved normalizing the error (difference in the modeled and measured current densities) by the measured current density, which skewed the results by placing a large weight on the small current density data. Second, the flow rates of feed gases are held at threshold values for $i < 0.1$ A cm^{-2}, so that that the

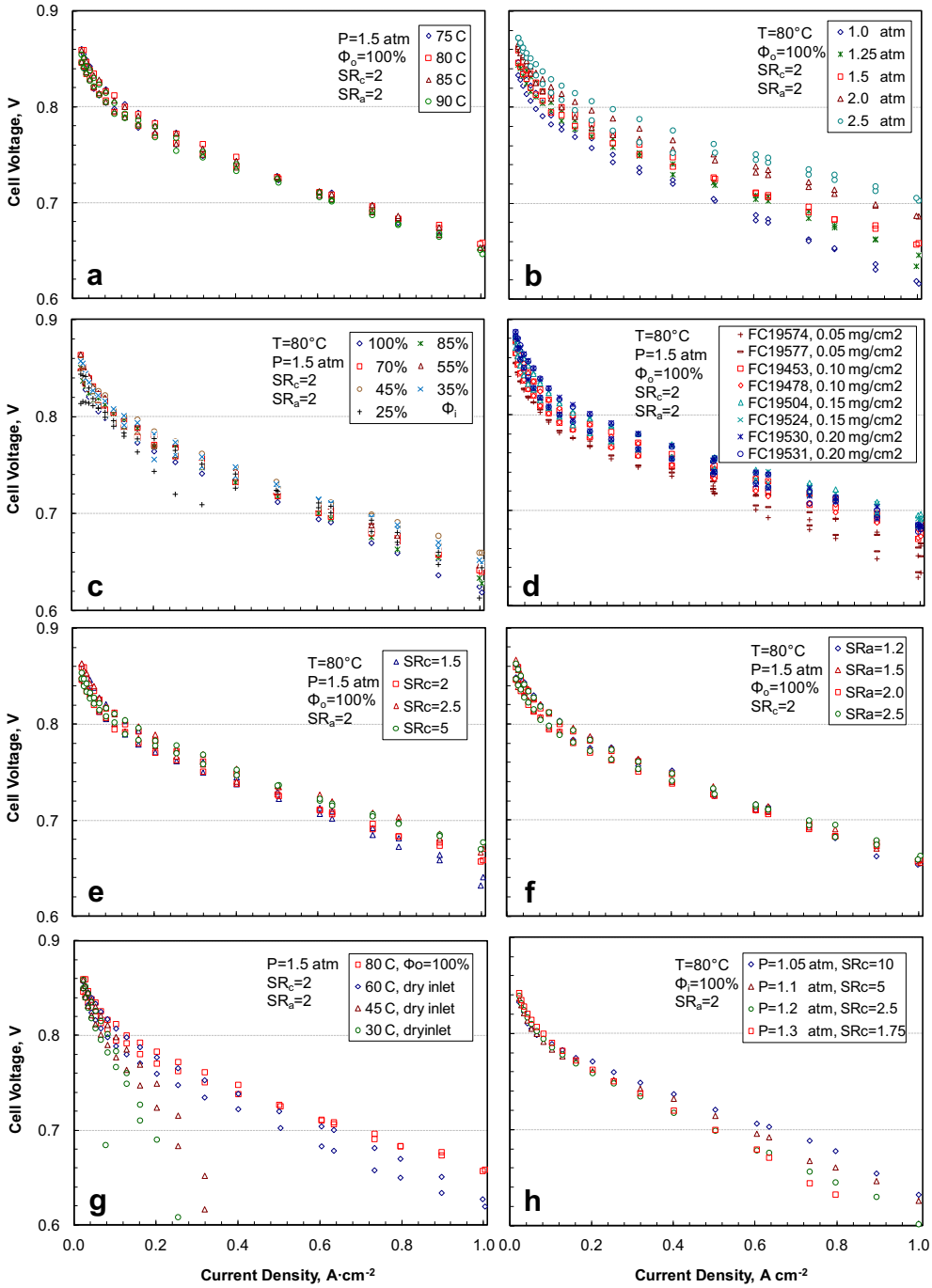

Fig. 1. GDS polarization curves with 2-min hold at each data point. Excluding Fig. 1d, all data taken on the reference cell with 0.103 mg cm^{-2} Pt loading in the cathode. Data for both upscans and downscans included.

Table 3
Cell characterization and performance data, all activities measured at 0.9 V IR-corrected cell voltage, 80 °C and 100% RH.

Cell Designation	19,574	19,577	19,453	19,478	19,504	19,524	19530	19531
Pt Loading, mg cm^{-2}	0.054	0.054	0.103	0.103	0.146	0.146	0.186	0.186
ECSA, $m^2_{Pt}.g^{-1}$	12.4	12.6	9.8	9.8	9.2	8.4	7.2	7.0
SEF, $cm^2_{Pt}cm^{-2}$	6.7	6.8	10.1	10.1	13.4	12.2	13.4	13
Catalyst Layer Thickness, mm	0.16 ± 0.018		0.32 ± 0.034		0.47 ± 0.048		0.61 ± 0.061	
H_2 Crossover, mA cm^{-2}	3.2	3.1	2.8	2.9	3.0	2.4	3.5	3.1
Short Resistance, Ω cm^2	588	267	933	664	182	216	340	379
Absolute Activity, mA cm^{-2}	11.3	13.5	17.6	18.8	23.5	23.3	25.5	24.1
Mass Activity, A mg^{-1}_{Pt}	0.21	0.25	0.17	0.18	0.16	0.16	0.14	0.13
Specific Activity, mA cm^{-2}_{Pt}	1.69	1.99	1.74	1.86	1.75	1.91	1.90	1.85

anode/cathode stoichiometries and exit dew points are different from those for $i > 0.1$ A cm^{-2}. Finally, the crossover current (i_x) can be a significant fraction of the total current for $i < 0.05$ A cm^{-2} but we did not specifically measure the RH dependence of i_x. We emphasize, however, that whereas the $i < 0.1$ A cm^{-2} data were not included in determining the ORR rate constants, they were considered in the subsequent evaluation of the kinetic model.

We represented the cell voltage (E) at the measured current density (i) in terms of the Nernst potential (E_N) calculated at the cell temperature (T) and the partial pressures (P) of H_2 and O_2, the cathode overpotential for ORR (η), and the Ohmic drop due to HFR (R_Ω).

$$E = E_N - iR_\Omega - \eta \quad [1]$$

$$E_N = E_0 + \frac{RT}{nF}\ln\left(\frac{P_{H_2}P_{O_2}^{1/2}}{\Phi}\right) \quad [2]$$

where E_0 is the standard potential for the fuel cell reaction assuming that the product water is liquid, Φ is the relative humidity (1 for 100% RH), and n equals 2.

$$E_0 = 1.23 + 0.000833(T - 298) \quad [3]$$

We neglect the small anode overpotential for the facile hydrogen oxidation reaction [10] and assume that the sluggish oxygen reduction reaction on cathode follows the Tafel equation with a single Tafel slope over the cathode potential range of interest.

$$i + i_x = i_0 A_{Pt} L_{Pt} P_{O_2}^{\gamma} \Phi^{\beta} \exp\left(\frac{\alpha nF}{RT}\eta\right) \quad [4]$$

where i_x is the hydrogen crossover current density, i_0 is the exchange current density (A.cm$_{Pt}^{-2}$), A_{Pt} is the electrochemically active surface area (ECSA, cm$_{Pt}^2$.mg^{-1}), L_{Pt} is the Pt loading (mg cm^{-2}), γ is the order with respect to O_2 partial pressure, Φ is the relative humidity, β is the order with respect to Φ, and α is the transfer coefficient. It is assumed that H_2 that crosses over undergoes $H_2 = 2H^+ + 2e^-$ half–cell reaction on the cathode catalyst, produces a mixed cathode potential, and leads to an internal cathodic current density (i_x).

3.1. Cell-averaged kinetics

We investigated the cell ORR kinetics by using the average H_2 and O_2 partial pressures across the cell (see Appendix 1). We found that the ORR overpotentials correlated better with the RH at cell exit rather than the inlet or average RH values. We formulated a stepwise procedure for determining γ, i_0, α, and β. We first determined γ by using the average polarization data in Series 2 at 80 °C, 50% H_2 and O_2 utilizations, and 100% RH at cell exit. For these conditions, Fig. 2a presents the ORR overpotential as a function of the current density for different air inlet pressures in the Series 2 tests. Fig. 2b indicates that the data in Fig. 2a are well correlated if the current density is scaled by $P_{O_2}^{-\gamma}$ with a γ of 0.36. Here, $P_{O_2}^{\gamma}$ represents the average partial pressure of O_2 in the channel, and is calculated by accounting for the pressure drop (ΔP) in the flow field and the O_2 consumption. The following correlation, developed from the measured inlet pressure in tests in which the exit pressure was 1 atm, was used to estimate ΔP (kPa) in terms of the gas volumetric flow rate ($\dot{V}$ in m^3 s^{-1}, superscripts a and c denote anode and cathode, respectively).

$$\Delta P^a = 1.6 + 1.3 \times 10^5 \dot{V} + 1.2 \times 10^9 \dot{V}^2$$

$$\Delta P^c = 1.8 + 2.3 \times 10^5 \dot{V} + 5.9 \times 10^9 \dot{V}^2 \quad [5]$$

In the second step, we investigated the temperature dependence of i_0 by analyzing the Series 1 data at 75, 80, 85 and 90 °C, with 50% H_2 and O_2 utilizations and 100% RH at cell exit, see Fig. 3a. We included the Series 2 data for 1, 1.25, 2 and 2.5 atm inlet pressures by using the γ values determined in the first step. We correlated the data, plotted as semi-logs in Fig. 3b, with straight lines and estimated α from the slope and i_0 from the intercept as per the following equation ($\Phi = 1$).

$$\eta = \frac{RT}{\alpha nF}\ln\left[(i + i_x)P_{O_2}^{-\gamma}\right] - \frac{RT}{\alpha nF}\ln\left(i_0 A_{Pt} L_{Pt} \Phi^{\beta}\right) \quad [6]$$

Fig. 3b presents the estimated i_0 as a function of 1/T and leads to the following Arrhenius correlation with an activation energy (E_{O_2}) of 57.7 kJ mol^{-1} for the ORR.

$$i_0 = i_{or}\exp\left[-\frac{E_{O_2}}{R}\left(\frac{1}{T} - \frac{1}{T_r}\right)\right] \quad [7]$$

where i_{or} is the exchange current density at the reference temperature ($T_r = 353$ K).

The third step consisted of investigating the RH dependence of the ORR. Fig. 4a presents the ORR overpotentials in the Series 3 tests for different exit RH at 80 °C and in the Series 2 tests for 1, 1.25, 2 and 2.5 atm inlet pressures. As per Eq. (6), we fitted the data with straight lines on semi-log axes and used the slopes to determine α as a function of Φ, see Fig. 4b.

$$\alpha = \frac{0.4665}{1 + 0.0926\Phi} \quad [8]$$

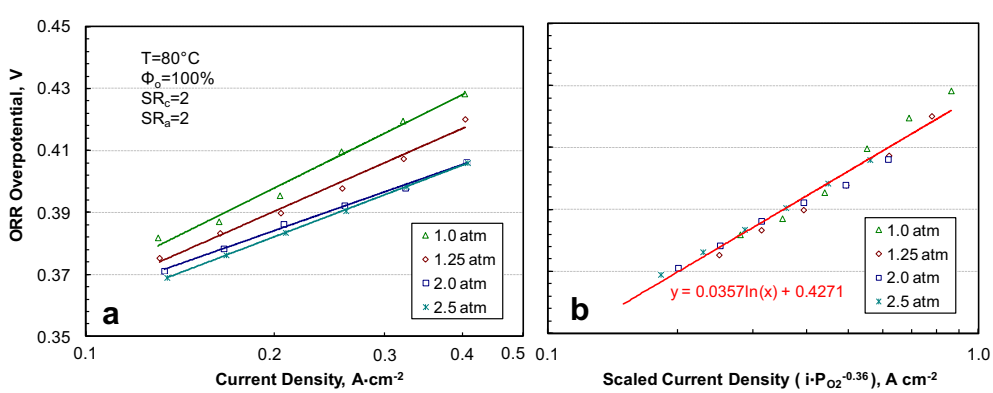

Fig. 2. Derived cell-averaged ORR overpotentials in series 2 data (a) and determination of the order with respect to P_{O_2} (b).

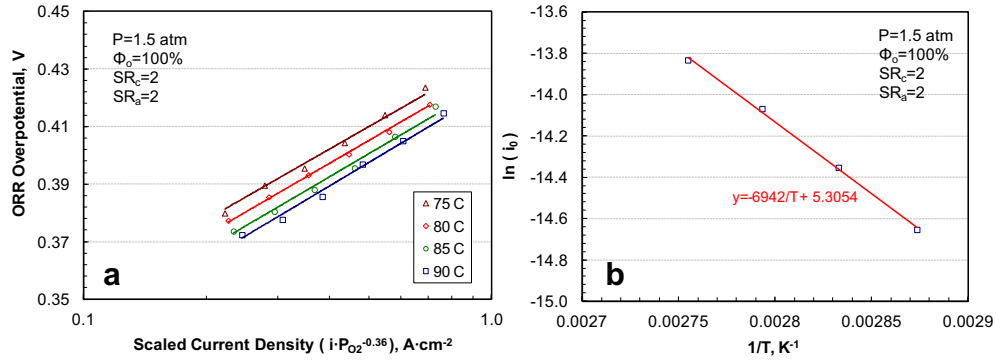

Fig. 3. Derived cell-averaged ORR overpotentials in series 1 data (a) and determination of the activation energy E_{O_2} for temperature dependence (b)

We used the intercepts in Fig. 4a to determine $i_0\Phi^{\beta}$ and these are presented in Fig. 4c. The power law fit in Fig. 4c leads to the following estimates for i_{or} (A.cm$_{Pt}^{-2}$) and β.

$$i_{0r} = 5.7 \times 10^{-7}, \quad \beta = 1.3. \qquad [9]$$

3.2. Local ORR kinetics

Whereas the above correlation for the average ORR kinetic rate is useful for characterizing the cell performance, it is desirable to have the ability to estimate the ORR overpotentials for the local values of i, T, P_{O_2}, and Φ. For this purpose, we developed a simple one-dimensional model to estimate the local values of i,P_{O_2}, P_{H_2} and Φ from the measured cell polarization curves. The model solves the following set of equations for anode and cathode pressures and for molar flow rates ($\dot{N}$) of H_2, O_2 and H_2O (subscript w) in the anode (superscript a) and cathode (superscript c) channels considering the source terms for the electrochemical reactions and water transport flux (J_w^m) across the membrane (superscript m) by electro-osmotic drag and diffusion (normal direction y).

$$\frac{dP^c}{dx} = -\frac{\Delta P^c}{L} \qquad [10]$$

$$\frac{dP^a}{dx} = -\frac{\Delta P^a}{L} \qquad [11]$$

$$\frac{d\dot{N}_{O_2}^c}{dx} = \left(\frac{i+i_x}{4F}\right)W_m \qquad [12]$$

$$\frac{d\dot{N}_w^c}{dx} = -\left(\frac{i+i_x}{2F}+J_w^m\right)W_m \qquad [13]$$

$$\frac{d\dot{N}_{H_2}^a}{dx} = -\left(\frac{i+i_x}{2F}\right)W_m \qquad [14]$$

$$\frac{d\dot{N}_w^a}{dx} = -J_w^m W_m \qquad [15]$$

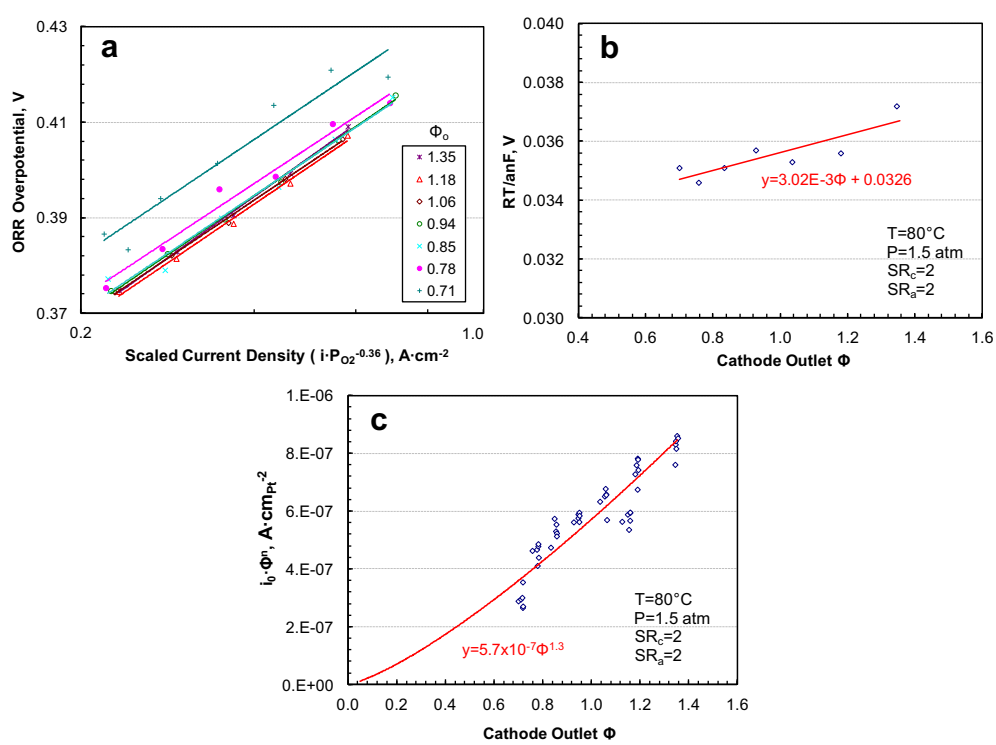

Fig. 4. Derived cell-averaged ORR overpotentials in series 3 data (a) and determination of the transfer coefficient, α (b) and the order with respect to RH, β (c).

The following auxiliary equations define J_w^m and relate P_{O_2}, P_{H_2} and Φ to the molar flow rates. Also, the current density i is given by Eq. (4).

$$J_w^m = \beta_\lambda\left(\frac{i}{F}\right) - \left(\frac{\rho_m}{EW}\right) D_\lambda \frac{\partial\lambda}{\partial y} \quad [16]$$

$$\dot{N}_{ws}^c = \frac{P_s}{P_c - P_s}\sum_{i\neq w}\dot{N}_i^c \quad [17]$$

$$\dot{N}_{ws}^a = \frac{P_s}{P_a - P_s}\sum_{i\neq w}\dot{N}_i^a \quad [18]$$

$$\Phi^c = \frac{\dot{N}_w^c}{\dot{N}_{ws}^c} = \frac{P_w^c}{P_s} \quad [19]$$

$$\Phi^a = \frac{\dot{N}_w^a}{\dot{N}_{ws}^a} = \frac{P_w^a}{P_s} \quad [20]$$

$$P_{H_2} = \frac{\dot{N}_{H_2}^a}{\sum \dot{N}_i^a} P^a \quad [21]$$

$$P_{O_2} = \frac{\dot{N}_{O_2}^c}{\sum \dot{N}_i^c} P^c \quad [22]$$

The following equation is used to calculate λ (λ^c or λ^a) as a function of Φ (Φ^c of Φ^a).

$$\lambda = \begin{cases} 23.82\Phi^4 - 28.53\Phi^3 + 8.36\Phi^2 + 5.92\Phi + 0.1 & (\Phi \le 1) \\ 9.67 + 2.8(\Phi - 1) & (\Phi \le 3) \\ 15.27 & (\Phi > 3) \end{cases} \quad [23]$$

In the above equations, H_2 flows in the anode channel along the x direction (L is the total length) whereas air flows in the cathode channel along the −x direction, superscript s represents saturation, λ is the water uptake in the membrane, ρ_m (2000 kg m^{-3}) and EW (850) are the membrane density and equivalent weight, and W_m is the membrane width. Note that P_s is the saturation pressure of water vapor and is a function of temperature only. Similarly, $\dot{N}_{ws}^c$ and $\dot{N}_{ws}^a$ are the molar flow rates of saturated water vapor and are related to P_s through Eqs. (17) and (18).

For expediency, we assumed that the electro-osmotic drag coefficient ($\beta_\lambda = 1$) and the water diffusion coefficient ($D_\lambda = 1.5 \times 10^{-6}$ cm^2 s^{-1}) are constant, so that Eq. (16) can be integrated analytically to obtain the λ profile and hence the water transport flux J_w^m across the membrane.

$$J_w^m = \beta_\lambda\left(\frac{i}{F}\right) - \left(\frac{\rho_m}{EW}\right)\left(\frac{D_\lambda}{\delta_m}\right)(\lambda^c - \lambda^a) \quad [24]$$

where δ_m is the membrane thickness.

A simple first-order finite-difference scheme was used to integrate Eqs. (10)–(15) simultaneously. We marched from anode inlet ($x = 0$) to anode outlet, i.e., the equations were integrated in the forward flow direction for the anode stream and in the backward flow direction for the cathode stream. The required boundary conditions for the anode stream were determined from the known molar flow rates of H_2 and H_2O in the anode feed gas. The required boundary conditions for the cathode stream are unknown and had to be determined iteratively. Our approach was to use a hybrid method, combining steepest descent with quasi-Newton update technique, to determine $\dot{N}_{O_2}^c$ and $\dot{N}_w^c$ at $x = 0$ such that $\dot{N}_{O_2}^c$ and $\dot{N}_w^c$ calculated by solving Eqs. (10)–(15) at cathode inlet match the experimental values (control variables).

We used an optimizer to determine the combination of i_{or}, E_{O_2}, and β that minimizes the root mean square difference between the measured and modeled current densities normalized by the measured current density in Series 1-3 data. The parameters were allowed to vary over a wide range: 5×10^{-8}–5×10^{-6} A cm$_{Pt}^{-2}$ for i_{or}, 20–80 kJ mol^{-1} for E_{O_2}, and 0.25–2.5 for β. Attempts to vary α proved unsuccessful because of convergence problems arising from the extreme sensitivity of the calculated overpotentials to α. It was also not possible to vary γ because, over the range of pressures for which the data were available, the calculated overpotentials were far less sensitive to γ than to other parameters. For these reasons, we retained Eq. (8) for α and kept γ at 0.36. We used a sequential quadratic programming technique for solving nonlinear constrained optimization problems. The following were the initial values of the various parameters appearing in Eq. (4) as determined by the optimizer: $i_{or} = 6.8 \times 10^{-7}$ A cm$_{Pt}^{-2}$, $E_{O_2} = 39.5$ kJ mol^{-1}, and $\beta = 0.9$. In a follow-on attempt, β was allowed to vary linearly with Φ since subsequent analysis suggested a stronger dependence of ORR kinetics on RH under dry conditions than can be explained with a constant β. The optimized value of β is given by the following linear function.

$$\beta = \begin{cases} 0.9 + 1.5(0.65 - \Phi) & \Phi < 0.65 \\ 0.9 & \Phi \ge 0.65 \end{cases} \quad [25]$$

For illustrative purposes, Appendix 2 shows the calculated profiles of i, P_{O_2}, P_{H_2} and Φ in Run 1.2 at 0.4 A cm^{-2}.

Fig. 5 compares the measured and modeled cell current density with the above parameters. It includes data from the tests in Series 1, 2 and 3 with different T, P and RH. All these tests were run with 50% H_2 and O_2 utilizations and a Pt loading of 0.103 mg cm^{-2} in the cathode and 0.05 mg cm^{-2} in the anode. For the data included in Fig. 5, the standard deviation (s) between the modeled (i_m) and measured (i_d) current densities is 22.1 mA cm^{-2} and the correlation coefficient (R^2) is 0.993.

Even though a direct comparison between the ORR kinetic parameters derived here for the ternary PtCoMn/NSTF with those reported in the literature for Pt/C is not meaningful because of the different catalysts (alloy vs. monometallic, polycrystalline thin-film

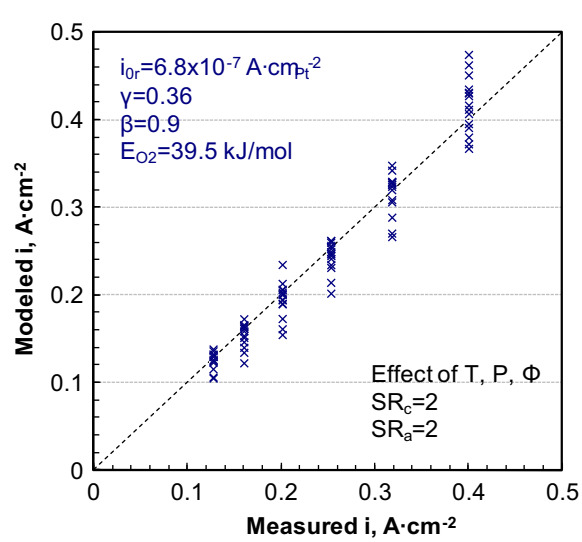

Fig. 5. Test of the local ORR kinetic correlation against data from series 1, 2 and 3.

vs. crystalline nanoparticles, nm vs. μm curvature, etc) and supports (organic vs. carbon, whiskers vs. particles, etc), it may be useful to discuss the associated trends. The PtCoMn/NSTF system shows a small RH dependence of the Tafel slope ($2.303RT/\alpha nF$) that at 80 °C decreases from 82 mV/decade for 100% RH to 78.5 mV/decade for 50% RH. The Pt/C system has a constant Tafel slope, 65 ± 2 mV/decade [11,14], although dependence of α on RH has been observed at 120 °C [15]. The pre-exponential term in Eq. (4), however, varies as $\Phi^{0.9}$ for PtCoMn/NSTF, whereas Pt/C shows no dependence on RH for $\Phi > 0.75$ but significant reduction for $\Phi < 50$–60% [16] possibly due to its effect on the H^+ concentration in the ionomer under very dry conditions ($\lambda < 2$–4). The PtCoMn/NSTF system has no ionomer in the catalyst layer other than the membrane material that partially fills the voids between the catalyst-coated whiskers when the CCM is formed. Also, the ORR kinetics on PtCoMn/NSTF shows smaller dependence on P_{O_2} (γ of 0.36 vs. 0.54) and temperature (activation energy of 39.5 kJ/mol vs. 67 kJ/mol) than Pt/C [17,18], possibly implying different rate-controlling steps in the overall mechanism [10].

The graphs in Fig. 6 show the validity of the kinetic parameters with respect to single variables, i.e., temperature (and RH) in Fig. 6a (Series 1 data), pressure (and RH) in Fig. 6b (Series 2 data), and RH in Fig. 6c (Series 3 data). Fig. 6 shows reasonable match between the model and data if i_{or} is slightly adjusted (by −4% to 6%) to account for variations in measured polarizations in the different series of tests (see Fig. 11). The standard deviation and R^2 are 13.1 mA cm^{-2} and 0.9977 for data with varying temperatures, 22.5 mA cm^{-2} and 0.9928 for data with varying pressures, and 22 mA cm^{-2} and 0.996 for data with varying relative humidities.

Fig. 7 tests the applicability of the model parameters in capturing the effects of cathode and anode stoichiometry. It includes data from the tests in Series 5 and 6, which were not used in determining the optimum choice of the ORR kinetic parameters. We found that i_{or} has to be increased by ~15% at $SR_c = 5$ and ~40% at $SR_c = 10$ (Fig. 8b) in order to get a good match between the model and the data ($s = 34$ mA cm^{-2}, $R^2 = 0.9836$). This increase in i_{or} at high SR_c may be related to the resultant high pressure drop that enhances air flow under the lands in the serpentine flow field. It has been suggested that this enhanced air flow assists in removing the liquid water from the GDL under the land, relieves liquid saturation in the cathode catalyst layer, and thereby improves the catalyst activity [19]. We determined an empirical factor (f) that describes the enhancement in i_{or} as a function of the cell cathode stoichiometry and the local current density.

$$f = 1 + (f_1(SR) - 1) f_2(i)$$
$$f_1(SR) = \begin{cases} 1.4 & SR_c > 10 \\ 1.0 + 0.0033(SR_c - 2)^2 + 0.0233(SR_c - 2) & SR_c > 1.75 \end{cases}$$
$$f_2(i) = \begin{cases} 1 & i > 0.125 \\ \dfrac{i}{0.125} & i \le 0.125 \end{cases} \qquad [26]$$

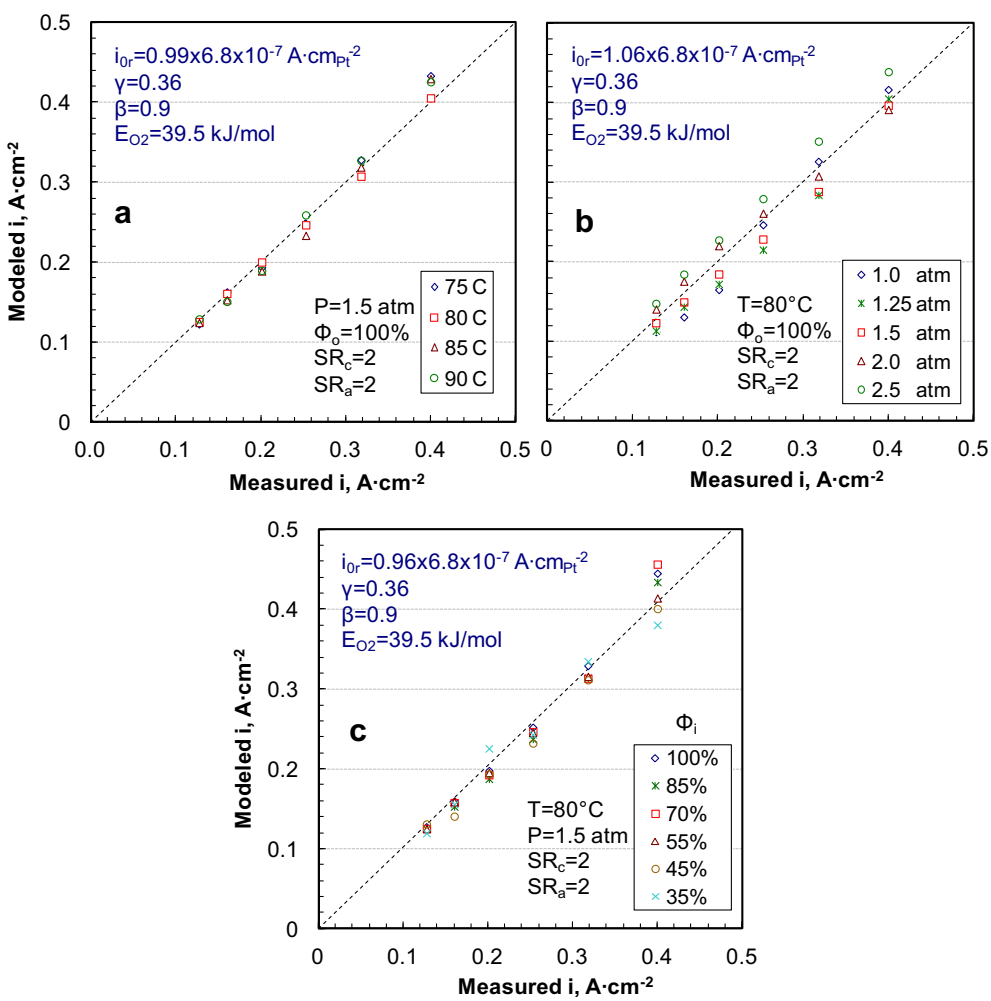

Fig. 6. Test of the local ORR kinetic correlation against series 1 data with varying temperature (a), series 2 data with varying pressure (b) and series 3 data with varying RH (c).

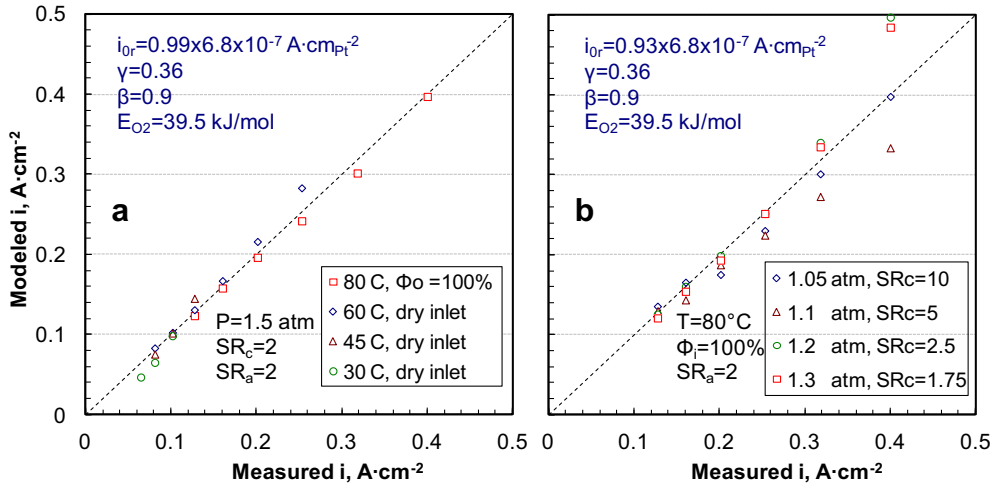

Fig. 7. Test of the local ORR kinetic correlation against series 5 data with varying cathode stoichiometry (a), and series 6 data with varying anode stoichiometry (b).

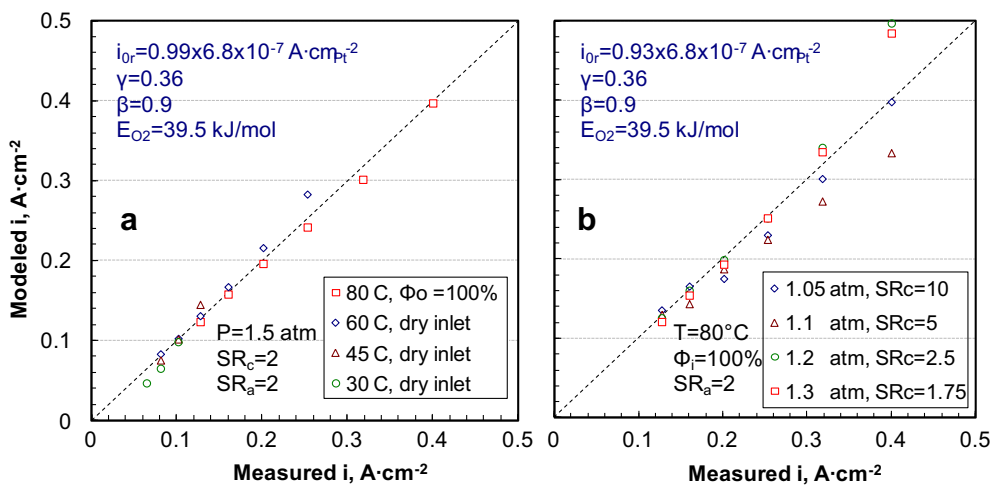

Fig. 8. Test of the local ORR kinetic correlation against series 7 data for low cell temperatures (a), and series 8 data for low pressures (b).

In our interpretation, whereas the kinetic parameters α, β, γ, i_{or} and E_{O_2} are unique to the PtCoMn/NSTF catalyst, the factor f is specific to the flow field and is likely to change with a different cell design.

As expected, the match between the model and data is better in Fig. 7b ($s = 9$ mA cm^{-2}, $R^2 = 0.9989$) than in Fig. 7a since the anode stoichiometry influences the ORR kinetics only indirectly, i.e., through water balance.

Fig. 8a provides a test of the applicability of the ORR kinetic parameters at low temperatures that the cell may experience during startup (Series 7 data) with dry feeds. The comparison is restricted to 0.1 A.cm^{-2} at 30 °C, 0.15 A.cm^{-2} at 45 °C, and 0.25

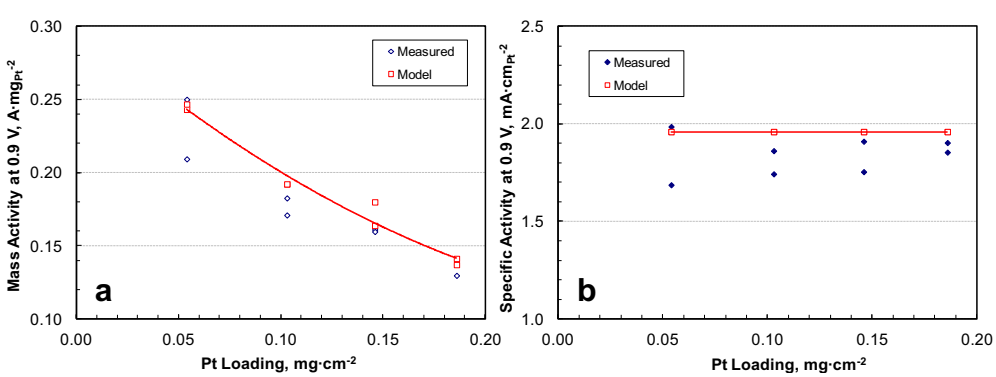

Fig. 9. Model validation against measured mass activities and specific activities for the cells with different Pt loadings.

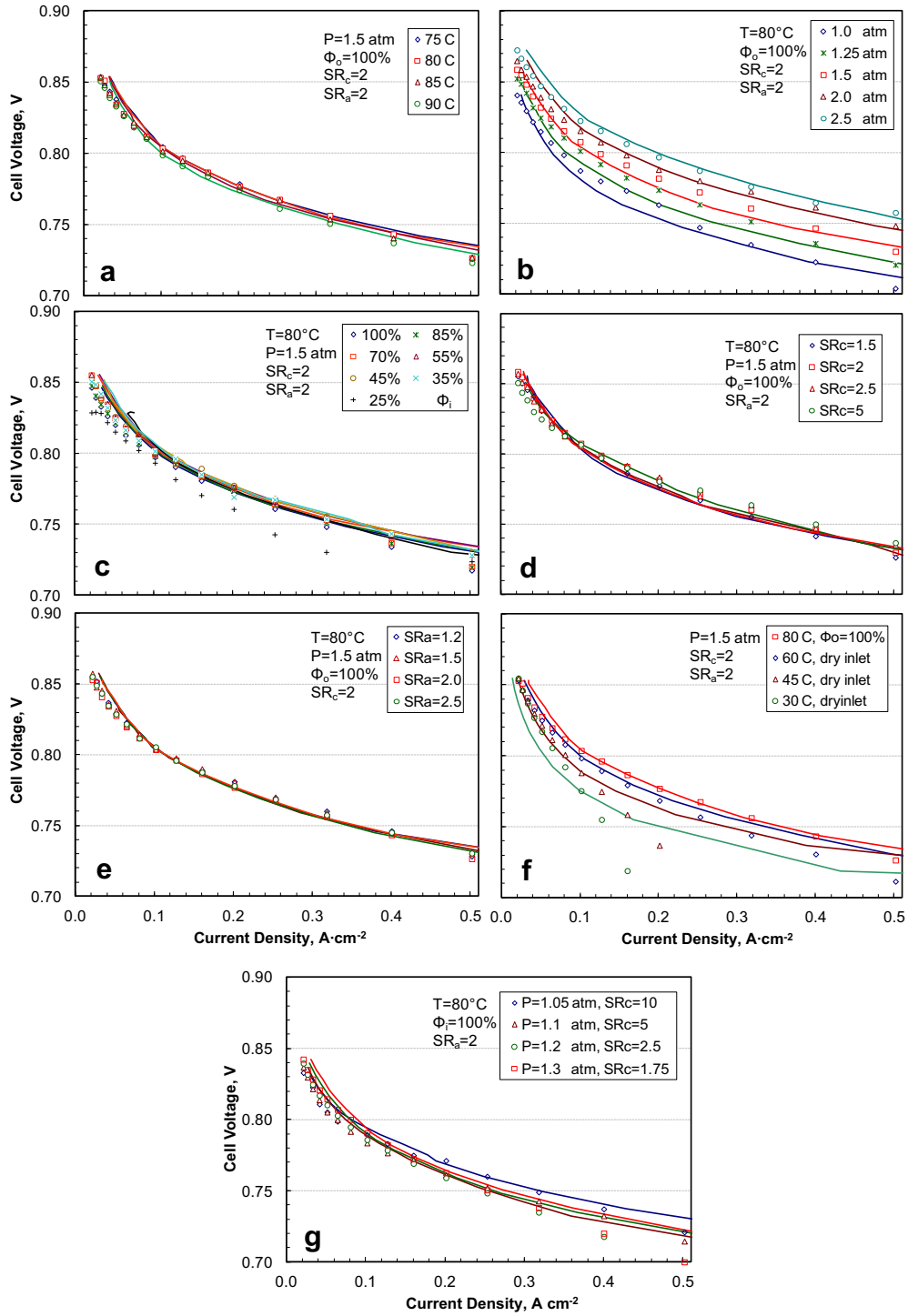

Fig. 10. Model validation against polarization data on the reference cell for different T (a), P (b), RH (c), SR_c (d), SR_a(e), cold temperatures (f), and low pressures and high SR_c (g).

A.cm^{-2} at 60 °C since the mass transfer effects are evident at higher current densities at these temperatures. The data in Fig. 8a suggest that an activation energy of 39.5 kJ mol^{-1} adequately reflects the effect of temperature on ORR kinetics over the range of 30–90 °C ($s = 2.3$ mA cm^{-2}, $R^2 = 0.9959$).

Fig. 8b measures the "goodness" of the correlation for low pressure and high-SR data (Series 8 for idling conditions, 100% inlet RH). We see that the empirically derived f function adequately describes the enhancement in i_{or} at high stoichiometries.

3.3. Discussion of the results

Fig. 9a compares the mass activities measured during Series 4 tests with the current densities calculated from our model for 0.9 V IR-corrected cell voltage, $P_{O_2} = 1$ atm, and $\Phi = 1$. As stated earlier, the measured mass activities correspond to current densities measured 20 min after holding the cell at 0.9 V. Fig. 9b gives a similar comparison between the modeled and measured specific current densities. Fig. 9a and b include data from cells (pairs) with

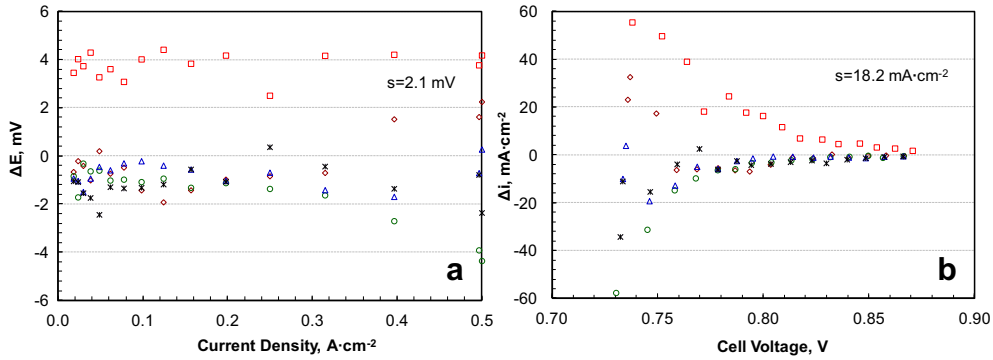

Fig. 11. Variability in data from six repeats of tests in series 1, 2, 3, 4, 5 and 6 at reference conditions. All data from the reference cell with 0.103 mg cm^{-2} Pt in the cathode.

different Pt loadings. The favorable comparisons suggest that the ORR kinetic parameters (α, β and γ) can be used for PtCoMn/NSTF cathode catalysts with different Pt loadings if the variation in ECSA with Pt loading is taken into account.

Fig. 10 compares the modeled and measured polarization curves for the seven series of tests conducted on the reference cell. There is generally a good agreement between the modeled and measured cell voltages for current densities between 0.1 and 0.4 A.cm^{-2} except under very dry conditions, such as at 25% RH in Series 3 data, where there is additional voltage loss due to membrane dry-out. The discrepancy at higher current densities is attributed to mass transfer effects that will be analyzed in a follow-on paper. The mass transfer effects (possible catalyst layer flooding) are evident even at 0.1 A.cm^{-2} for cell temperatures below 45 °C (Series 7 data). The model correctly calculates the ordering of cell voltages with temperature (E(75 °C) > E(80–85 °C) > E(90 °C)) in Series 2 data. The model also calculates the increase in cell voltage with increase in SR_c for current densities between 0.1 and 0.4 A cm^{-2}, as measured in Series 5 data, and the observed reordering in cell voltages with respect to SR_c at lower current densities.

It is worth mentioning that the inlet pressure is the control variable except at low pressures (1–1.05 atm data) and high current densities or high cathode stoichiometries. In these instances, the outlet pressure is 1 atm and the inlet pressure is raised to produce the specified flow rate, see Eq. (5). Thus, the cell inlet pressure for the Series 8 data identified as 1.05 atm and $SR_c = 10$ can be higher than for the 1.2 and 1.3 atm, lower SR_c data, and may show higher cell voltages at current densities >0.1 A.cm^{-2}.

The cell voltages calculated from our correlation are within 5–10 mV of the measured values for current densities lower than 0.1 A cm^{-2}. In taking the polarization data at current densities between 0.02 and 0.1 A cm^{-2}, the H_2 and air flow rates were held at the set threshold values, 100 slpm for H_2 and 185 slpm for air. Cell operation at high air stoichiometry results in the relative humidity staying close to the inlet value, which can be as low as 40% in the Series 2 test at 75 °C and the Series 5 test at 1.5 nominal SR_c (see Table 2). We found much better agreement between the model and low-RH data for <0.1 A.cm^{-2} current densities if β, the order with respect to RH, is allowed to increase for $\Phi < 0.65$, as in Eq. (25).

The polarization data for the reference conditions in Table 1 were taken at different times in Series 1, 2, 3, 5 and 6 tests. We have used these data to establish the variability in our measurements. Fig. 11a indicates that the measured cell voltages at the reference conditions are reproducible within ±5 mV and have a standard deviation of 2.1 mV over the current density range of 0.02–0.5 A cm^{-2}. Fig. 11b presents the corresponding variation in the current density estimated by using a Tafel slope of 82 mV/decade in Eq. (4). The standard deviation for the estimated current densities is 18.2 mA cm^{-2} over a range of 0.73–0.87 V IR-corrected cell voltages. Our kinetic correlation has a comparable standard deviation of 9–22.5 mA cm^{-2} for all the data taken in Series 1, 2, 3, 5 and 6 tests along with ±6% variation in i_{or}. Thus, the "goodness" of the ORR correlation is consistent with the accuracy and reproducibility of the polarization data.

Further work is required to verify and improve the kinetic model. The model reliability will improve with more accurate and reproducible data (see Fig. 11). Additional data are needed to test the RH dependence of ORR kinetics (α and β) and the effect of high SR_c on i_o.

4. Summary and conclusions

The kinetics of the oxygen reduction reaction (ORR) on PtCoMn/NSTF can be correlated with the following simple Tafel equation with a single value of the transfer coefficient (α).

$$i + i_x = i_0 A_{Pt} L_{Pt} P_{O_2}^{\gamma} \Phi^{\beta} \exp\left(\frac{\alpha n F}{RT}\eta\right)$$

$$i_0 = i_{or} f(SR_c) \exp\left[-\frac{E_{O_2}}{R}\left(\frac{1}{T} - \frac{1}{T_r}\right)\right],$$

$$i_{0r} = 6.8x10^{-7} \mathrm{A.cm}_{Pt}^{-2}, \quad E_{O_2} = 39.5 \mathrm{kJ.mol}^{-1}, \quad T_r = 353\mathrm{K}$$

$$\gamma = 0.36$$

$$\beta = \begin{cases} 0.9 + 1.5(0.65 - \Phi) & \Phi < 0.65 \\ 0.9 & \Phi \geq 0.65 \end{cases}$$

$$\alpha = \frac{0.4665}{1 + 0.0926\Phi}$$

$$f = 1. + (f_1(SR) - 1) f_2(i)$$

$$f_1(SR) = \begin{cases} 1.4 & SR_c > 10 \\ 1.0 + 0.0033(SR_c - 2)^2 + 0.0233(SR_c - 2) & SR_c > 1.75 \end{cases}$$

$$f_2(i) = \begin{cases} 1 & i > 0.125 \\ \dfrac{i}{0.125} & i \leq 0.125 \end{cases}$$

We regard the kinetic parameters i_{or}, α, β, γ and E_{O_2} as specific to the PtCoMn/NSTF catalyst tested and the factor f that accounts for the increase in catalyst activity at high stoichiometries as an attribute

of the flowfield design. The ECSA (A_{Pt}) is a function of the Pt loading in the cathode catalyst, decreasing from 12.5 ± 0.1 $m^2\ g^{-1}$ for 0.054 mg cm^{-2} Pt loading to 7.11 ± 0.1 $m^2\ g^{-1}$ for 0.186 mg cm^{-2} Pt loading. The order (β) for RH dependence increases sharply for Φ below 0.65. The above choice of the kinetic parameters is consistent with the cell polarization data at 30–90 °C, 0.1–0.5 atm P_{O_2}, 35–100% RH (Φ) and 0.054–0.186 mg cm^{-2} Pt loading (L_{Pt}) and also with the mass activity and specific activity measurements in H_2/O_2 at 0.9 V IR-corrected cell voltage, 80 °C, 1 atm P_{H_2} and P_{O_2}, and 100% RH.

Acknowledgments

This work was supported by the Fuel Cell Technologies Program of the U.S. Department of Energy's Office of Energy Efficiency and Renewable Energy. Dr. Nancy Garland and Mr. Jason Marcinkoski are the DOE's program managers for this work. The authors thank Dr. Romesh Kumar for many helpful discussions.

Appendix 1. Average H_2 and O_2 pressures in the Cell

$$P_{O_2} = \frac{P^c_{in}}{2}\left[X^c_{O_2,in} + \left(1 - \frac{\Delta P^c}{P^c_{in}}\right)X^c_{O_2,o}\right]$$

$$\dot{N}^c_{O_2,o} = \dot{N}^c_{O_2,in}(1 - 1/SR_c)$$

$$X^c_{O_2} = \frac{\dot{N}^c_{O_2}}{\sum \dot{N}^c_i}$$

$$P_{H_2} = \frac{P^a_{in}}{2}\left[X^a_{H_2,in} + \left(1 - \frac{\Delta P^a}{P^a_{in}}\right)X^a_{H_2,o}\right]$$

$$\dot{N}^a_{H_2,o} = \dot{N}^a_{H_2,in}(1 - 1/SR_a)$$

$$X^a_{H_2} = \frac{\dot{N}^a_{H_2}}{\sum \dot{N}^a_i}$$

where X is the mole fraction and the subscripts *in* and *o* denote the cell inlet and outlet, respectively.

Appendix 2. Representative axial profiles

Fig. 12 presents a sample of the calculated axial profiles of i, P_{O_2}, P_{H_2} and Φ for Run 1.2 at 0.4 A.cm^{-2}. The anode H_2 stream in Fig. 12 flows from left to right while the cathode air stream flows from right to left.

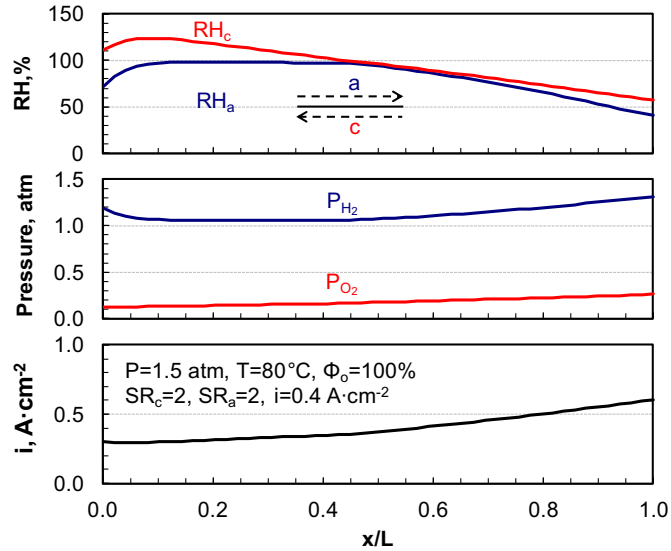

Fig. 12. Sample axial profiles of i, P_{O_2}, P_{H_2} and Φ in run 1.2 at 0.4 A cm^{-2}.

References

[1] M.K. Debe, in: W. Vielstich, A. Lamm, H.A. Gasteiger (Eds.), Handbook of fuel cells: Fundamentals, Technology and Applications, vol. 3, John Wiley & Sons, Chichester, England, 2003.
[2] M.K. Debe, A.K. Schmoeckel, R.T. Atanasoski, G.D. Vernstrom, Paper 64 Presented at the fuel cell Seminar, Palm Springs, CA, 14–18 Nov. 2005.
[3] M.K. Debe, A.K. Schmoeckel, S.M. Hendricks, G.D. Vernstrom, G.M. Haugen, R.T. Atanasoski, ECS Trans. 1 (8) (2006) 51.
[4] M.K. Debe, A.K. Schmoeckel, G.D. Vernstrom, R. Atanasoski, J. Power Sources 161 (2006) 1002–1011.
[5] A.J. Steinbach, K. Noda, M.K. Debe, ECS Trans. 3 (1) (2006) 835–853.
[6] A. Bonakadarpour, K. Stevens, G.D. Vernstrom, R. Atanasoski, A.K. Schmoeckel, M.K. Debe, J.R. Dahn, Electrochim. Acta 53 (2007) 688–694.
[7] M.K. Debe, A.K. Schmoeckel, R.T. Atanasoski, G.D. Vernstrom, Paper 583 Presented at the fuel cell Seminar, Honolulu, HI, 13–17 Nov. 2006.
[8] D. van der Vliet, C. Wang, M. Debe, R. Atanasoski, N. Markovic, V. Stamenkovic, Electrochim. Acta 56 (2011) 8695–8699.
[9] D. van der Vliet, D. Strmcnik, C. Wang, R. Atanasoski, M. Debe, N. Markovic, V. Stamenkovic, Multimetallic catalysts for the oxygen reduction reaction, 216th ECS Meeting, Vienna, Oct. 2009.
[10] M.K. Debe, J. Electrochem. Soc. 159 (1) (2012) B54–B67.
[11] K.C. Neyerlin, W. Gu, J. Jorne, H.A. Gasteiger, J. Electrochem. Soc. 153 (2007) A1955–A1963.
[12] A.J. Steinbach, C.V. Hamilton, M.K. Debe, ECS Trans. 11 (1) (2007) 889–897.
[13] F.T. Wagner, H.A. Gasteiger, R. Makharia, K.C. Neyerlin, E.L. Thompson, S.G. Yan, ECS Trans. 3 (1) (2006) 19.
[14] K.C. Neyerlin, W. Gu, J. Jorne, H.A. Gasteiger, J. Electrochem. Soc. 154 (2007) B631–B635.
[15] H. Xu, Y. Song, H.R. Kunz, J.M. Fenton, J. Electrochem. Soc. 152 (2005) A1828–A1836.
[16] K.C. Neyerlin, H.A. Gasteiger, C.K. Mittelsteadt, J. Jorne, W. Gu, J. Electrochem. Soc. 152 (2005) A1073–A1080.
[17] K.C. Neyerlin, W. Gu, J. Jorne, H.A. Gasteiger, J. Electrochem. Soc. 154 (2007) B279–B287.
[18] H.A. Gasteiger, J.E. Panels, S.G. Yan, J. Power Sources 154 (2007) 162–171.
[19] H. Yamada, T. Hatanaka, H. Murata, Y. Morimoto, J. Electrochem. Soc. 153 (2006) A1748–A1754.